




Quasi-two-dimensional antiferromagnetism with large magnetocrystalline anisotropy in the half-filled square-planar iridate $\text{Cs}_2\text{Na}_2\text{IrO}_4$

Roumita Roy  and Sudipta Kanungo ^{*}*School of Physical Sciences, Indian Institute of Technology Goa, Goa-403401, India* (Received 5 January 2023; revised 7 August 2023; accepted 22 September 2023; published 6 October 2023)

A rare class of square-planar iridate, $\text{Cs}_2\text{Na}_2\text{IrO}_4$, where isolated IrO_4 moieties are oriented orthogonally in the consecutive lattice planes, has been investigated using first-principles calculations. Microscopic magnetic exchange interactions and Wannier function analysis reveals the quasi-two-dimensional antiferromagnetic ground state with moderate mean-field transition temperature, in spite of the absence of long-range structural connectivity via IrO_4 moieties. Further magnetic interactions pointed out possible canting of the Ir spins in a complex manner, due to the orthogonally oriented IrO_4 planes. The estimated magnetocrystalline anisotropy is significantly large, which is further accentuated by Os doping due to the modification of the electronic configurations and electronic structure of the valence and conduction bands. The phonon modes analysis confirms very weak spin-phonon coupling and reveals the possible mechanism for the evolution of orthogonally oriented IrO_4 moieties. The energetics of the muon active sites has been identified to guide the experimental measurements.

DOI: [10.1103/PhysRevB.108.155110](https://doi.org/10.1103/PhysRevB.108.155110)

I. INTRODUCTION

In the last decade, iridates have attracted major attention as emerging quantum materials due to their delicate interplay amongst various energy scales. Recent developments in the field of iridates include the proximal observance of Kitaev spin liquid in $\text{Ag}_3\text{LiIr}_2\text{O}_6$ [1,2], spin-orbit excitons in $\text{Sr}_3\text{Ir}_2\text{O}_3\text{F}_2$ [3], Weyl phase in pyrochlore $\text{Eu}_2\text{Ir}_2\text{O}_7$ [4], and so on. The local structural environment of the iridium atom is one of the crucial factors in dictating the properties of such systems. However, the major focus of iridates is on the systems with octahedral coordination of surrounding O atoms, to form either a corner-shared perovskite type structure or an edge-shared honeycomb structure, where the standard J_{eff} states [5] can be realized in the $\text{Ir-}t_{2g}$ manifold in the presence of strong spin-orbit coupling (SOC). The other vastly studied iridates are formed in the pyrochlore structure where Ir is in the tetrahedral coordination of four O atoms. The Ir $5d$ orbitals here, split into $e - t_2$ manifolds. In both of the above cases, Ir prefers to be in the low spin state. Unlike various $3d$ complexes, for example, cuprates [6], nickelates [7], Fe oxides [8], etc., iridates rarely exhibit square-planar coordination due to the fact that heavy elements, viz., $5d$ series, always prefer to remain in a low spin configuration, under regular circumstances. However, recently, square-planar coordination in $4d$ (Pd) and $5d$ (Pt) systems are emerging as quantum materials that exhibit topological quantum phases [9] and there are a lot more scopes for the iridates as well.

The first case where the iridates have been reported to occur in a square-planar environment is in A_4IrO_4 [10–12] with $\text{A} = \text{Na}, \text{K}, \text{and Cs}$, where Ir is in an intermediate spin state of $S = \frac{3}{2}$ with antiferromagnetic (AFM) ordering at $T_N = 25 \text{ K}$

[13,14], due to the interplay of Coulomb correlations and crystal field effect with giant magnetic anisotropy energy [15]. The sister compound of this family has been synthesized [16] with 50% Cs substitution at the Na site, which yields $\text{Cs}_2\text{Na}_2\text{IrO}_4$ and is isoelectronic with the former. Usually the reported square-planar coordination for a heavy element such as Pd, Pt, etc., is in d^8 or d^9 electronic configuration with a high spin state [17–20]. Moreover, the above-mentioned square-planar cases are either edge or corner shared among each other. An interesting fact is that in $\text{Cs}_2\text{Na}_2\text{IrO}_4$, the IrO_4 square-planar entities are completely isolated in nature, without any cooperative structural connectivity. In addition, the IrO_4 square-planar plaquettes are not orientated in the same plane and the structure consists of two orthogonally oriented IrO_4 square-planar plaquettes, which is remarkably different from Na_4IrO_4 . Such striking structural changes visible only due to isoelectronic substitution at the A site cation is in itself quite fascinating.

In this study we thus aim to understand the structure-property relationship of this rare example of a half-filled iridate in an orthogonally oriented isolated square-planar coordinated material using first-principles density functional theory (DFT) calculations. We obtained very interesting electronic and magnetic ground states with reduced dimensionality, along with substantial anisotropy. We also provide a qualitative understanding of the orthogonally oriented IrO_4 square planes from phonon analysis.

II. CALCULATION METHODOLOGY

The DFT calculations were performed within the plane-wave based basis set of 500 eV cutoff on a pseudopotential framework with the Perdew-Burke-Ernzerhof (PBE) [21] exchange-correlation functional as implemented in the Vienna *ab initio* simulation package (VASP) [22,23]. The effect of

^{*}sudipta@iitgoa.ac.in

electron-electron Coulomb correlations was taken into account via on-site Hubbard U [24,25]. The standard value of U_{eff} ($U - J_H$) for the Ir $5d$ states as per literature, is ≈ 2 eV [26–29]. However, due to the presence of isolated IrO_4 entities it is intuitive to expect that a comparatively large value of U will be appropriate to describe the current system. To cross-verify, we performed the electronic and magnetic structure calculations with a wide spectrum of U_{eff} values as reported in Supplemental Material Figs. S1 and S2 and Table T2 [30]. The resulting effects are discussed in detail in the subsequent sections. The SOC effect has been incorporated as a relativistic correction term in the noncollinear mode, as implemented in VASP [31]. The $4 \times 8 \times 6$ k mesh in the Brillouin zone (BZ) was used for self-consistent calculations. The experimentally obtained structures were optimized by relaxing the atomic positions towards equilibrium until the Hellmann-Feynman forces become less than 0.001 eV/Å, keeping the lattice parameters fixed at the experimentally obtained values. The low-energy Hamiltonian was acquired via the Wannier function basis [32] using a downfolding technique. Only the Ir $5d$ orbitals were kept as the active degrees of freedom, integrating out all other degrees of freedom in constructing the low-energy Hamiltonian. The dynamical stability of the crystal structures has been investigated via phonon density of states (DOS), using the open-source PHONOPY code [33] employing the same energy cutoff or k -mesh grid in each of the respective cases. The phonon results are also cross-checked with the supercell calculations. The muon active sites have been calculated by the addition of positively charged H atomic sites, which mimics the $+\mu$ present in the structure. We further optimized the positions to get the most preferred location of the muons. During optimization only the position of the H atom was changed without altering the position of other sites.

III. CRYSTAL STRUCTURE

$\text{Cs}_2\text{Na}_2\text{IrO}_4$ crystallizes in a monoclinic structure (space group $C2/m$) and consists of layered IrO_4 planes, along the c direction as shown in Fig. 1(a). The interesting feature of this crystal structure is that the IrO_4 planes in each alternating layer are perpendicular to each other. For example, in one layer the IrO_4 planes lie in the ac plane (viz., site I) and in the next layer they are oriented perpendicular to the former, i.e., in the ab plane (viz., site II), as shown in Figs. 1(b) and 1(c), respectively. These orthogonally oriented IrO_4 planes are the major deviation in the crystal structure from its parent counterpart material Na_4IrO_4 .

Secondly, unlike other iridate systems, the structure of $\text{Cs}_2\text{Na}_2\text{IrO}_4$ is highly porous and lacks the long-range cooperative structural connectivity. The IrO_4 square planes are completely isolated moieties and are not connected with each other via oxygen ligands, which has been seen in most of the cases. In spite of the fact that the Na and Cs atoms are also not connected with O or Ir atoms, replacing 50% of the Na atoms by Cs atoms rotates half of the IrO_4 planes orthogonally to each other. The electronic origin of such peculiar behavior is elaborated later. The IrO_4 square planes are slightly distorted in terms of both bond lengths and angles and the deviation is more prominent for the case of the IrO_4 in the ac plane than

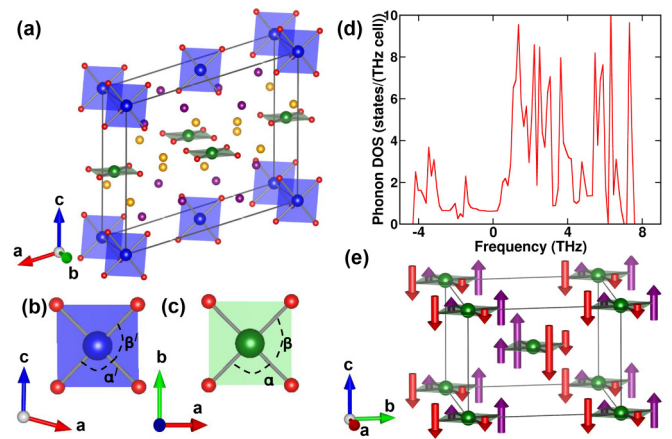


FIG. 1. (a) Crystal structure of $\text{Cs}_2\text{Na}_2\text{IrO}_4$, where violet, orange, and red spheres represent Cs, Na, and O atoms, respectively. Ir atoms and corresponding IrO_4 square planes in the ab and ac planes are represented by green and blue spheres and polyhedra, respectively. (b) and (c) show a planar view of IrO_4 moieties in the ac (site I) and ab (site II) planes, respectively. $\angle\text{O-Ir-O}$ bond angles have been marked as α, β and α', β' respectively, for ab and ac planar IrO_4 . (d) Phonon DOS for the structure obtained by replacement of 50% of Na atoms in Na_4IrO_4 with isoelectronic Cs. (e) The phonon displacement eigenvectors corresponding to the negative frequency modes are shown at the various O sites in each IrO_4 plane.

in the ab plane. The average Ir-O bond lengths are 1.93 and 1.94 Å, respectively, for Ir at site I and site II, respectively, as obtained from the GGA+ U structural optimization. The $\angle\text{O-Ir-O}$ bond angles are also deviated ($\angle\alpha' = 88.07^\circ$, $\angle\beta' = 91.93^\circ$, $\angle\alpha = 90.01^\circ$, and $\angle\beta = 89.99^\circ$) from the ideal 90° .

To further analyze the structure we began with the crystal structure of Na_4IrO_4 and replaced 50% of the Na atoms with Cs atoms and performed structural optimization of the atomic positions and the symmetries to generate the $\text{Cs}_2\text{Na}_2\text{IrO}_4$ structure. Post structural optimization we found that all the IrO_4 planes were still oriented along the same direction parallel to each other and did not capture the orthogonally oriented IrO_4 feature. Additionally, we calculated the phonon DOS of the $\text{Cs}_2\text{Na}_2\text{IrO}_4$ structure generated from the Na_4IrO_4 structure, as shown in Fig. 1(d). The presence of negative-frequency modes in the phonon DOS suggested that the structure was dynamically unstable. The corresponding phonon modes that are leading to the instability in the structure were further examined as shown in Fig. 1(e). The arrows at each O site represent the phonon displacement modes (eigenvectors). On looking at the displacement vectors we find that in each plane the centrally located Ir atoms hardly experience any displacement. In contrast to that, the diagonally placed O atoms of each IrO_4 plane experience displacement along opposite directions parallel to the crystallographic c axis, as marked by the up and down arrows in Fig. 1(e). This results in the IrO_4 plane rotating orthogonal to the ab plane. The point to be noted here is that the magnitude of the rotating eigenvectors is comparatively less in one IrO_4 layer than in the consecutive one. This further suggests that the IrO_4 square planes in each alternate layer will rotate orthogonal to the

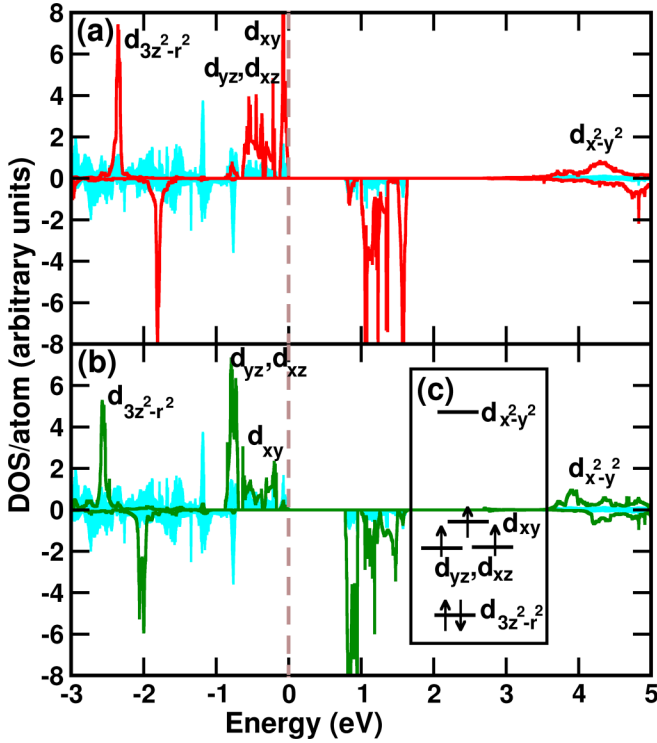


FIG. 2. The calculated GGA+ U ($U_{\text{eff}} = 2$ eV) Ir d orbital projected DOS are shown for Ir sites in (a) the ac (red) and (b) the ab (green) planes, respectively. The corresponding O p orbital projected DOS is shown in cyan (light) lines for the respective planes in (a) and (b). The Fermi energy is set at zero in the energy scale. (c) The energy-level diagram of Ir $5d$ orbitals is shown.

ab plane, thus leading to the unusual crystal structure of this compound.

IV. ELECTRONIC STRUCTURE

The calculated GGA+ U ($U_{\text{eff}} = 2$ eV) electronic structure is shown in Fig. 2. The Cs and Na are in the nominal +1 valence states with inert shell configuration, so the corresponding DOS are not shown in the specified energy range. The fivefold degeneracy of the Ir d orbitals is lifted as per the square-planar crystal field. Due to less repulsion along the out-of-plane direction, the $d_{3z^2-r^2}$ orbital lies at the bottom and is completely filled in both the spin channels as seen from the DOS. A point to be noted here is that the exchange splitting for $d_{3z^2-r^2}$ is much lower than the crystal field splitting. The double occupation of the $d_{3z^2-r^2}$ orbital is mostly due to the reduced electronic repulsion along the out-of-plane direction (z direction) and the presence of a_{1g} symmetry for the $4s$ and $d_{3z^2-r^2}$ orbitals in D_{4h} symmetry [8,34,35]. Figure 2 clearly depicts that the almost degenerate d_{yz} - d_{xz} orbitals and the d_{xy} orbitals lie close to E_f and are filled only in the majority spin channel. As expected, the $d_{x^2-y^2}$ orbitals lie very far away in the energy scale (around 4.5 eV above the E_f), and are completely empty in both spin channels. The calculated spin magnetic moment at the two different crystallographic Ir sites is mentioned in Table I. As shown in Table I, the value of the magnetic moment increases from 1.61 (1.63) to 1.86

TABLE I. The calculated spin magnetic moments for $\text{Cs}_2\text{Na}_2\text{IrO}_4$ at the two Ir sites for GGA+ U (with U_{eff} ranging from 0 to 3 eV). The values are mentioned in units of μ_B .

U_{eff} (eV)	Spin magnetic moment at Ir site (μ_B)	
	Site I	Site II
0	1.61	1.63
1	1.69	1.71
2	1.77	1.79
3	1.86	1.88

(1.88) at site I (II) with the increase in U_{eff} from 0 to 3 eV. Nevertheless, the total magnetic moment per formula unit remains unchanged at $3\mu_B/\text{f.u.}$, with the change in the value of Hubbard U_{eff} . From the occupation of the various d orbitals, calculated magnetic moments, and DOS we can state that the Ir atoms are in $(+4)5d^5$ configuration with an intermediate spin state of $S = \frac{3}{2}$. The $S = \frac{3}{2}$ spin state of the system is independent of the choice of Hubbard U . Considering $S = \frac{3}{2}$, the reduced spin magnetic moment at the Ir sites is due to the strong hybridization between Ir $5d$ and O $2p$, that results in the presence of a considerable amount of moment ($\sim 0.2\mu_B$) at the oxygen site as well. The electronic structure is further investigated by tailoring the Hubbard U_{eff} parameter and the corresponding DOS is shown in Supplemental Material Fig. S1 [30]. We find that an insulating gap is present even in the absence of U_{eff} , which increases with the enhancement of U_{eff} , as expected. The nature and the orbital occupancies of the DOS remains intact with the variation of U_{eff} from 0 to 3 eV. With this detailed analysis of the electronic structure and the magnetic moments as listed in Table I, we conclude that the charge and spin states also remain intact across an array of U_{eff} , which is crucial in establishing the robustness of the electronic structure of the system with respect to the choice of U_{eff} within a physically permissible range.

The band structure for GGA+ U (left panel) and GGA+ U +SOC (right panel) along the high-symmetry K points in the BZ are shown in Fig. 3. With the inclusion of SOC, we find very interesting changes in the band structures. The effect of SOC is rather strong in the conduction bands as compared to the valence bands. The top of the valence bands remains almost unaffected with the inclusion of SOC; however, the conduction bands get split up by breaking the band degeneracy in the presence of SOC. The bottommost of the conduction bands now become really flat and split up from the other two bands. As a result, the band gap is marginally reduced, in the presence of SOC. A point to be pondered here is that usually the effect of SOC in iridates is very strong; however, depending on the electronic configurations, that effect can be modulated. In the present case, Ir atoms are in d^5 - $S = \frac{3}{2}$ configuration, where all the orbital degrees of freedom are quenched, which usually reduces the impact of SOC. Nevertheless, even in this orbitally quenched situation we find that the effect of SOC is substantial in this material. Hence, it is expected that the effect of SOC in deriving the underlying magnetism would also be crucial and is discussed in the subsequent sections.

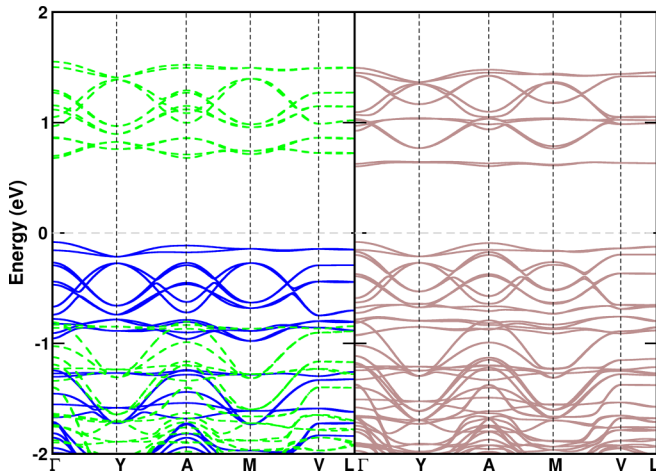


FIG. 3. Left: The calculated spin-resolved band structure calculated using GGA+ U ($U_{\text{eff}} = 2$ eV). The blue and green dotted curves represent the majority and minority spin channels, respectively. Right: The calculated band structure for GGA+ U ($U_{\text{eff}} = 2$ eV) + SOC (along the 110 axis).

V. MAGNETISM

To the best of our knowledge, there is no existing experimental study to understand the magnetic ordering of $\text{Cs}_2\text{Na}_2\text{IrO}_4$. In this section we thus aim to understand the microscopic detailing of the magnetism in this apparently unusual structured material. We have performed total energy calculations for various possible AFM spin configurations in addition to that of the fully polarized ferromagnetic (FM) configuration. Further, with the inclusion of SOC, noncollinearity was introduced, i.e., now the spins at the Ir sites were allowed to freely orient towards any crystallographic directions. From this arrangement we found that the Ir spins are canted with respect to the global coordinate axes. We investigated the total energy for various noncollinear spin configurations and also computed the magnetocrystalline anisotropy for the system.

TABLE II. The calculated (GGA+ U , with $U_{\text{eff}} = 2$ eV) magnetic exchange interactions (J 's) strengths and types are shown. The corresponding Ir-Ir distances are also mentioned.

Interactions	Ir-Ir distance (\AA)	Value (meV)	Type
J_1	6.65	0.11	AFM
J_2	6.67	0.07	FM
J_3	5.64	0.31	AFM

A. Magnetic exchange interactions

For a better understanding of the microscopic nature of magnetism in $\text{Cs}_2\text{Na}_2\text{IrO}_4$, we have evaluated the magnetic exchange interactions, connecting different nearest and next-nearest neighbor Ir sites. The magnetic exchange interaction paths as marked in Fig. 4(a), were calculated and tabulated in Table II. We utilized a methodology of obtaining the exchange interactions by mapping the DFT total energies of the system onto the corresponding generalized Heisenberg spin Hamiltonian of the form of $E^{\text{Tot}} = \sum_{ij} J_{ij} S_i S_j$ [36–38], where J_{ij} is the magnetic exchange interaction between the i th and j th sites and S_i and S_j are the effective spins at the corresponding sites; this methodology is well established [37,39–42] to provide qualitative measures of the magnetic exchange interactions in terms of magnitudes and signs. We took into consideration different collinear AFM spin configurations as pictorially shown in Supplemental Material Fig. S2 [30]. Regardless of the spin configuration, the magnetic moments at the Ir sites are almost equal, which indicates that the magnetic moments in $\text{Cs}_2\text{Na}_2\text{IrO}_4$ are very localized around the Ir sites. This is expected due to the absence of cooperative structural connectivity. Amongst them we found that the configuration in which the Ir atoms are aligned antiferromagnetically in each layer as well as along the global c axis (AFM3), has the lowest energy. The comparative energetics of the various spin configurations with the variation of U_{eff} is listed in Supplemental Material Table T1 [30]. We find that AFM3 (pictorial representation shown in Supplemental Material Fig. S2 [30]) has

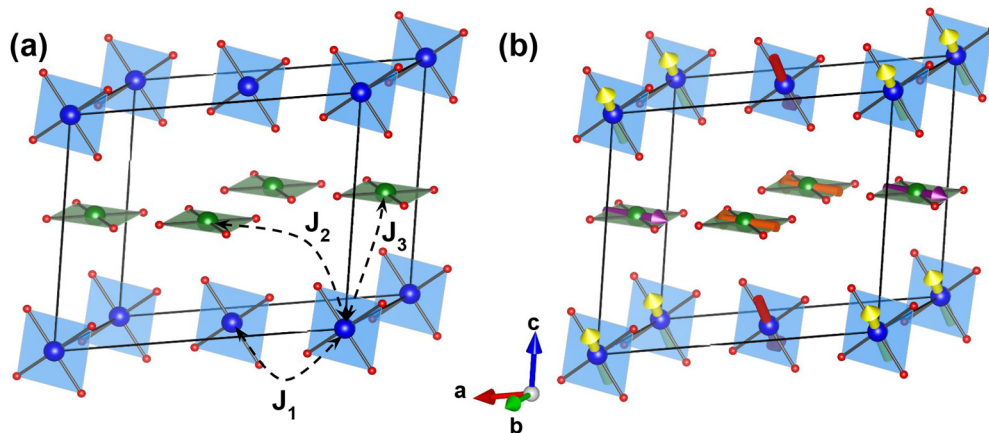


FIG. 4. (a) The magnetic exchange interaction paths J_1 , J_2 , and J_3 have been marked. (b) The ground state AFM magnetic configurations for GGA+ U +SOC ($U_{\text{eff}} = 2$ eV). The various spin directions at Ir sites are marked with different colored arrows. Color convention of the Ir atoms is the same as that of Fig. 1.

the lowest energy irrespective of the choice of U_{eff} . Moreover, the energy difference between the various spin configurations decreases with the increase in U_{eff} , which suggests the possibility of spin fluctuations in the low-temperature regime, which is important to explore in the future.

J_1 represents the interaction between two Ir atoms lying in the same plane, while J_2 and J_3 represent the exchange interactions between two orthogonally oriented Ir sites. We found that the exchange interaction between the orthogonally oriented Ir site, i.e., J_3 , is the strongest and almost three times stronger compared to that of J_1 , where both of these exchange interactions are AFM in nature. We also found a small FM type J_2 , which is negligible compared to others. The nature of the magnetic exchange interactions suggests that it is much stronger between the two orthogonally oriented IrO_4 moieties as compared to the parallel IrO_4 moieties. A point to be noted is that, due to the lack of cooperative structure, the magnetic exchange interaction strength is comparatively weak. Moreover, the magnetic interaction between Ir-Ir in the bc plane is almost three times stronger than the interaction strength in the ab plane and an order of magnitude higher than the interaction strength in the ac plane. Therefore, this material although structurally three dimensional, in terms of magnetic interaction strength is equivalent to quasi-two-dimensional in nature. The calculated mean-field transition temperature [43] from the calculated J 's is around 18 K, which is similar in order of magnitude to that of Na_4IrO_4 [13]. The above trend of exchange interactions is tested with the change in U_{eff} from 0 to 3 eV (as shown in Supplemental Material Table T2 [30]). As U_{eff} increases, the magnitude of the magnetic exchange interactions decreases, which is consistent with the decrease in the comparative energetics of different spin configurations as listed in Supplemental Material Table T1 [30]. Nevertheless, the relative strength of the different J 's remains broadly unaffected with the change in U_{eff} . Therefore, the quasi-two-dimensional description of the material remains valid irrespective of the applied U_{eff} values.

Since SOC has a significant effect on the electronic band structure, it is expected that SOC can induce noncollinearity in the Ir spins to stabilize the low-energy AFM ground state. Therefore, we reinvestigated the energetics of different AFM spin configurations in the presence of SOC via GGA+ U +SOC calculations and found that the nature of the lowest-energy AFM configuration remains unaltered as compared to the previously mentioned non-SOC results. However, due to the introduction of SOC, the Ir spins are now canted with respect to each other, as shown in Fig. 4(b). In each layer we see that the preferred spin orientation is along the direction of the IrO_4 plane. They, however, retain the AFM alignment between two such planes for a given layer.

The details of the nature of the relative magnetic interactions can be understood from the chemical perspective by Wannier functions [44,45] visualization. In Fig. 5 the Wannier functions for $\text{Cs}_2\text{Na}_2\text{IrO}_4$ have been shown, where the central part of the Wannier functions is shaped according to the plotted active Ir $5d$ characters and the tails situated at oxygen sites are shaped as per the integrated out orbitals. The Wannier function's weightage of the tails at neighboring atoms describes the strength of the interaction between the connected atomic sites. Figure 5 shows the central part is of

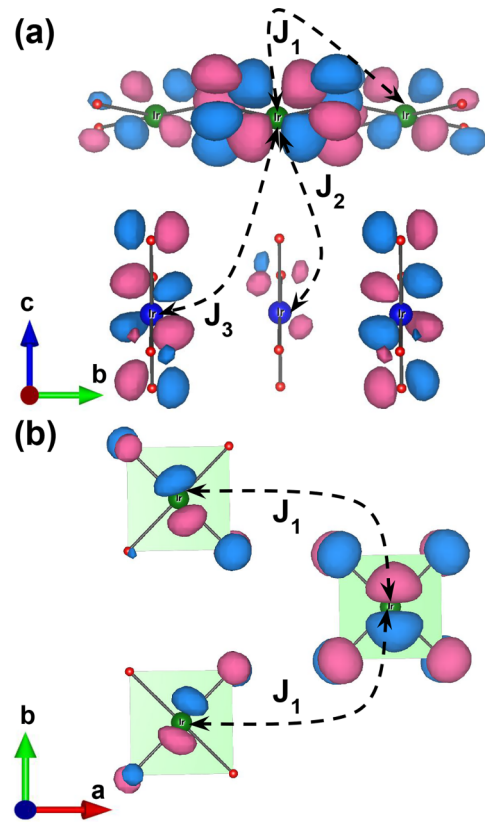


FIG. 5. The calculated Wannier functions for different exchange interaction paths are shown. The Ir $5d_{yz}$ Wannier orbitals centered at the Ir site are shown in the (a) bc and (b) ab projected planes. Pink and blue lobes represent isosurfaces with isovalues $+0.18$ and 0.18 , respectively. Color convention of the Ir and O atoms is the same as that of Fig. 1.

the Ir $5d_{yz}$ orbital character and the tails situated at different Ir and O sites indicate the strength of the interaction with the central Ir atom. In Fig. 5(a), we can see that J_3 is the strongest interaction amongst all due to the presence of the extended and large tail at the neighboring orthogonally oriented Ir sites, while J_2 is almost negligible as shown in Fig. 5(a). However, the J_1 interaction, which is in between two Ir sites, where IrO_4 is oriented in the same plane, has significant Wannier function tails, suggesting that J_1 is also significant in magnitude, which we found to be $1/3$ of the J_3 interaction. The Wannier function findings are consistent with the calculated values of the magnetic exchange interactions (J) as mentioned in Table II from *ab initio* total energy calculations.

B. Spin-phonon coupling

The presence of highly cooperative magnetic interactions and long-range magnetic ordering, in the absence of the structural connectivity lacking a cooperative network of magnetic sites (Ir in this case), is a very unlikely phenomena which we obtained in $\text{Cs}_2\text{Na}_2\text{IrO}_4$. Similar counterintuitive facts had been also observed experimentally in the parent compound Na_4IrO_4 , where the long-range AFM transition was noted at around 25 K. Ideally, in lattices without cooperative connectivity, it is unusual that spins at the lattice sites can

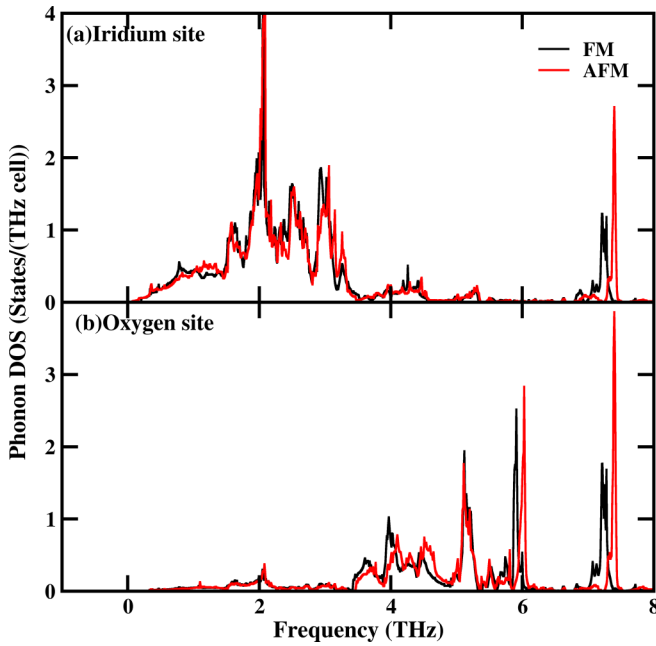


FIG. 6. Atom projected phonon density of states in FM (black line) and AFM (red line) configurations for the (a) Ir (site I) and (b) surrounding oxygen atoms.

build up long-range cooperative magnetic ordering. Contrary to this popular belief, in the case for the present compound $\text{Cs}_2\text{Na}_2\text{IrO}_4$, with isolated IrO_4 square-planar entities placed orthogonally with each other and an absence of long-range structural connectivity, we found long-range magnetic ordering, which suggests that the lattice and spin degrees of freedom are decoupled from each other. To prove this point, we have calculated the spin-phonon coupling for $\text{Cs}_2\text{Na}_2\text{IrO}_4$ by investigating the changes in the phonon density of states by changing spin configurations, i.e., FM and AFM spin configurations. The comparative analysis of the phonon DOS for the FM and ground state AFM configurations is shown for Ir atoms lying in the ac plane and the O atoms connected to the Ir atoms in the ac plane are shown in Figs. 6(a) and 6(b), respectively. From Figs. 6(a) and 6(b), we can clearly see that there are almost no changes in the phonon DOS by changing the spin orientations from FM to AFM, except for a few hard phonon modes at very high frequencies. Therefore, one can confirm that in this material the spin-lattice coupling is comparatively weak, which further ensures the stabilization of the long-range AFM ground state, despite the absence of long-range lattice connectivity.

C. Magnetocrystalline anisotropy

The effect of the SOC in the electronic structure and the emergence of spin canting has been investigated via GGA+ U +SOC calculations. It is expected that in an orbitally quenched electronic configuration where orbital magnetic moment is much less, the single-ion magnetocrystalline anisotropy is not very prominent. Since the crystal structure of this material is a unique layered kind without long-range connectivity, it is worth investigating the magnetocrystalline anisotropy (MCA) of this material. A point to be remembered

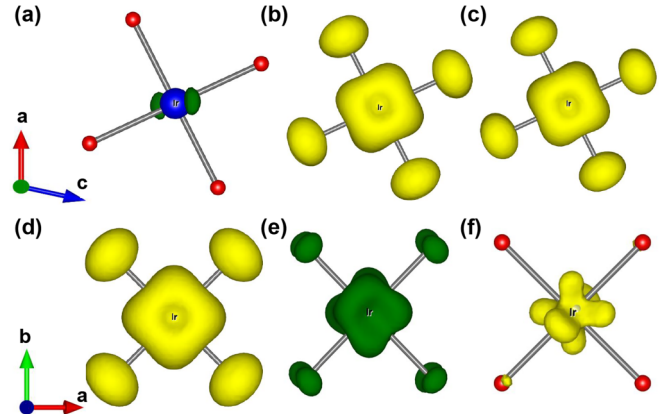


FIG. 7. (a)–(c) Magnetization density along m_x , m_y , and m_z for IrO_4 in the ac plane, respectively. (d)–(f) Magnetization density along m_x , m_y , and m_z for IrO_4 in the ab plane, respectively. The yellow and green lobes represent isosurface with positive and negative signs of magnetization, respectively.

is that a substantial out-of-plane MCA was also found in the parent compound Na_4IrO_4 and it was reported that the MCA could be further boosted up via appropriate doping at the Ir sites [14].

The MCA is referred to in terms of easy axis or easy plane; however, in this material due to the presence of two orthogonally oriented IrO_4 planes, the MCA description is more complex. We performed total energy calculations with different global spin quantization directions, and the values of MCA are listed in Table III. We found that the [110] Miller indices direction is energetically favorable by ≈ 10 meV/f.u. In the presence of SOC, the spin moments are split into m_x , m_y , and m_z projections and we found that the spin moments at Ir sites I and II experience a slight modification as shown in Table III. Under the influence of SOC, a part of the spin magnetic moment is transferred to its orbital counterpart. For heavier $5d$ systems such as Ir, the orbital moment is expected to have a very high value and in some cases it is reported to be twice the spin magnetic moment [5]. The value of the orbital magnetic moment, however, depends on the intricate electronic occupation of the system. In the present case we obtain the orbital magnetic moment for different spin quantization axes as shown Table III and one can clearly find that the orbital moment is of the order of 10–20% of the spin value. This highlights the significant quenching of the orbital moment due to the half-filled character in the $S = \frac{3}{2}$ spin state. Interestingly, if we look at the magnetization density at the different Ir sites, as shown in Fig. 7, the spin density is not exactly oriented in the global [110] direction for all Ir sites. This disparity is major because of the different orientations of the IrO_4 planes—one in the ab plane and another in the ac plane. From the magnetization density for Ir atoms that lie in the ac plane as shown in Figs. 7(a)–7(c), we find that in this case the magnetization is along the m_y and m_z directions. Similarly, in Figs. 7(d)–7(f), for the Ir atoms in the ab plane the major contribution of spins is along the m_x and m_y directions, which coincide with the global MCA direction.

TABLE III. The GGA+ U ($U_{\text{eff}} = 2$ eV)+SOC calculated magnetocrystalline anisotropy and the spin and orbital magnetic moments for $\text{Cs}_2\text{Na}_2\text{IrO}_4$ for various FM noncollinear configurations, where m_i and o_i (with $i = x, y, \text{ and } z$) represent the spin and orbital magnetic moments along the $x, y, \text{ and } z$ directions, respectively. The values of MCA and magnetic moments are mentioned in units of meV and μ_B , respectively.

Spin quantization directions	MCA/f.u. (meV)	Ir site I			Ir site II		
		m_x (o_x)	m_y (o_y)	m_z (o_z)	m_x (o_x)	m_y (o_y)	m_z (o_z)
001	12.10	0.07 (−0.01)	0.00 (0.00)	1.64 (0.23)	−0.19 (0.04)	0.00 (0.00)	1.61 (−0.04)
100	11.49	1.61 (0.05)	0.00 (0.00)	0.28 (−0.24)	1.61 (−0.04)	0.00 (0.00)	0.18 (0.04)
110	0.00	−0.09 (0.00)	1.14 (−0.06)	1.12 (0.10)	1.58 (−0.02)	−0.31 (−0.02)	0.11 (0.05)
101	11.82	1.05 (0.22)	0.00 (0.00)	1.21 (0.03)	1.06 (0.25)	0.00 (0.00)	1.24 (0.06)

The large value of MCA in $\text{Cs}_2\text{Na}_2\text{IrO}_4$ can be understood as an interplay of large SOC, electronic structure, and the influence of an unusual crystal structure. In heavier elements such as Ir, Os, etc., the large SOC strength contributes to the enhancement of MCA even in the scenario where the orbital moment is quenched. In $\text{Cs}_2\text{Na}_2\text{IrO}_4$, due to the presence of isolated IrO_4 moieties the magnetic moment is localized at the Ir site, which further paves the path for enhancement of MCA. Another factor that is to be taken into account is the low-symmetry square-planar coordination environment of the Ir atoms in this compound, which causes the d -level splitting to be much different compared to that of an octahedral environment. In the present compound the exchange splitting of the occupied d_{xy} orbital and the unoccupied $d_{yz} - d_{zx}$ orbital is very large; as a result, although the orbital moment is quenched at the Ir site, the MCA energy is substantial. Additionally, due to the presence of the two orthogonally oriented, isolated IrO_4 moieties, structurally this compound is also very anisotropic, which further enhances the MCA energy of this compound significantly. A large value of MCA in cases where the orbital moment is quenched has also been previously reported for the different $5d$ compounds [46–48]. We have calculated the MCA by varying the SOC strength, as shown in Supplemental Material Fig. S3 [30], which clearly indicates that the MCA varies quadratically with the SOC strength. A similar trend of MCA was also observed in the case of Na_4IrO_4 [15], which could be explained by the second-order perturbation theory.

The unique features of MCA in $\text{Cs}_2\text{Na}_2\text{IrO}_4$ motivates us to explore this family of compounds further. For the parent compound Na_4IrO_4 , it is known that replacing Ir by Re can drastically increase the MCA energy [14], therefore it is worth exploring a similar route for $\text{Cs}_2\text{Na}_2\text{IrO}_4$ as well, where the structural arrangement is even more complex. The motivation behind substitution at the Ir sites is to externally perturb the system such that there is a change in the position of the orbitals near the Fermi energy level so as to decrease the gap between the highest occupied orbital and the lowest unoccupied orbital, through which the MCA can be tuned. However, we found that the Re variant of the present compound does not form a dynamically stable structure with two orthogonally oriented ReO_4 square-planar entities. We have also cross-checked for the Os, Pt, as well as the isoelectronic Rh variant of $\text{Cs}_2\text{Na}_2\text{IrO}_4$ by optimizing the crystal structure. Nevertheless all of them show small negative frequencies in the phonon DOS as shown in Supplemental Material Fig. S4 [30]. This suggests that their structures are dynamically unstable.

However, the 50% Os doping at Ir sites forms a stable structure without any negative frequency modes, as shown in the phonon DOS in Fig. 8(b). All the Os atoms here prefer to occupy the same plane. We have also cross-checked the thermodynamic stability by calculating the temperature variation of free energy and entropy as shown in Fig. 8(c), which clearly confirms the stability of the $\text{Cs}_2\text{Na}_2\text{Ir}_{0.5}\text{Os}_{0.5}\text{O}_4$ compound. We also find that the square-planar geometry of the IrO_4 and OsO_4 planes is retained after substitution. From the orbital projected DOS in Fig. 8(a) we can conclude that Os is in +4 nominal valence state with $S = 1$ spin state. The calculated spin magnetic moments at the Ir and Os sites are $1.77\mu_B$ and $1.55\mu_B$, respectively. The induced magnetic moment at the O sites in the IrO_4 plane is $0.27\mu_B$, and that in the OsO_4 plane is at a much lower value of $0.12\mu_B$, thus suggesting a stronger hybridization of Ir with O, as compared to Os. Further calculations show that the MCA energy becomes as high as 21.39 meV/f.u. in the 50% Os-doped case and the preferential axis is along the [111] plane in contrast to [110].

The enhancement of MCA and the change in the easy quantization direction with Os substitution can be understood from the modification of the electronic structure due to the Os

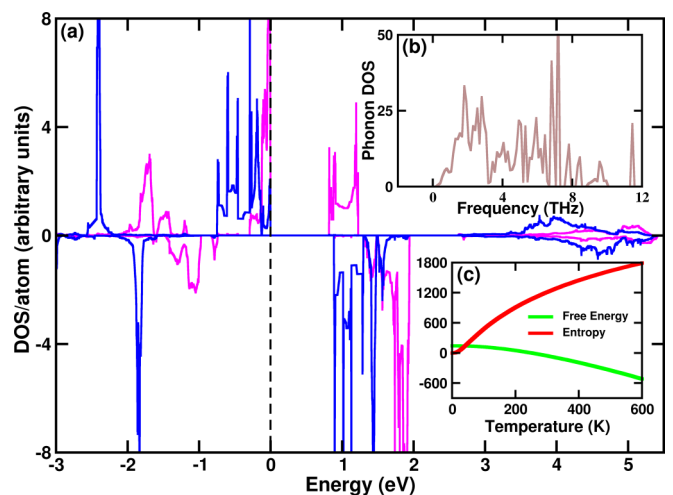


FIG. 8. (a) The GGA+ U ($U_{\text{eff}} = 2$ eV) orbital projected DOS for $\text{Cs}_2\text{Na}_2\text{Ir}_{0.5}\text{Os}_{0.5}\text{O}_4$, where blue and magenta represent Ir d and Os d states, respectively. The Fermi energy level has been set to zero. (b) represents the phonon DOS [states/(THz cell)] of $\text{Cs}_2\text{Na}_2\text{Ir}_{0.5}\text{Os}_{0.5}\text{O}_4$. (c) The entropy [J/(K mol)] and the Helmholtz free energy (kJ/mol) as a function of temperature represented by the red and green curves, respectively.

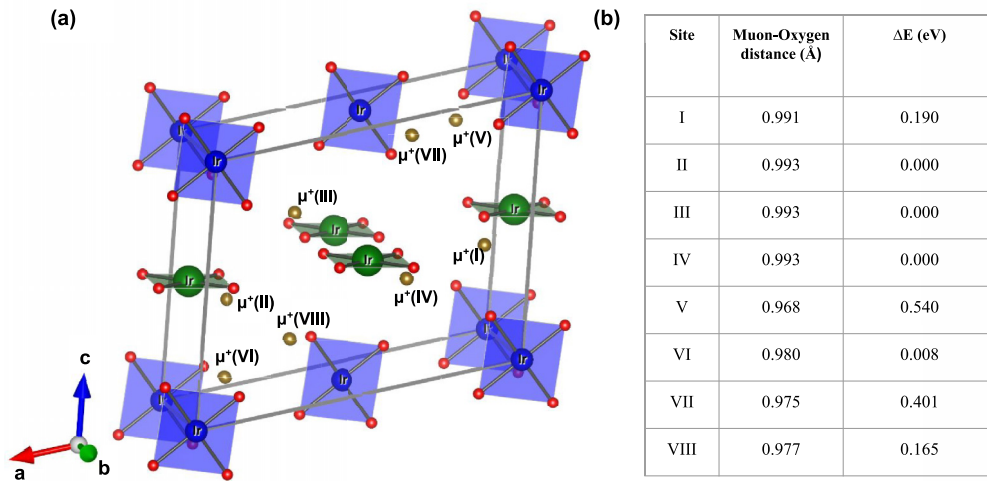


FIG. 9. (a) Eight μ^+ stopping sites for $\text{Cs}_2\text{Na}_2\text{IrO}_4$. Ir atoms in the ab plane are represented by green spheres and those in the ac plane by blue spheres. IrO_4 square planes are represented by blue and green polyhedra for the ac and ab planes, respectively. O atoms and μ^+ are represented by red and brown spheres, respectively. (b) Relative energy of each μ^+ stopping site and distance with the nearest oxygen atom.

substitution. The electronic structure shows that the unoccupied Ir d states of $\text{Cs}_2\text{Na}_2\text{Ir}_{0.5}\text{Os}_{0.5}\text{O}_4$ in the minority spin channel move closer to the Fermi energy, which decreases the exchange splitting as compared to that of the Ir d states of the $\text{Cs}_2\text{Na}_2\text{IrO}_4$ case. This in turn allows for the enhancement of MCA. Moreover, from our calculations we found that the origin of the change of easy axis from [110] to [111], is mainly driven by the electronic structure and electronic configurations contribution. In $\text{Cs}_2\text{Na}_2\text{Ir}_{0.5}\text{Os}_{0.5}\text{O}_4$, Ir is in +4 nominal valence state with $5d^5$ electronic configuration ($S = \frac{3}{2}$), whereas Os with one electron less is in +4 nominal valence state and has $5d^4$ electronic configuration ($S = 1$). Therefore in the case of the Os-substituted system, the d_{z^2} orbital is completely filled by two electrons, whereas $d_{yz} - d_{zx}$ is half-filled with one majority spin electron at each level and the d_{xy} is completely empty in both spin channels. Hence in this case, the smallest energy gap amongst the occupied and unoccupied levels occurs between the filled $d_{yz} - d_{zx}$ and the empty d_{xy} in the same spin channel, whereas, for the case of $\text{Cs}_2\text{Na}_2\text{IrO}_4$, it is in between the occupied majority spin channel of d_{xy} and the empty minority spin channel of $d_{yz} - d_{zx}$. A point to be noted here is that the stated energy gap for $\text{Cs}_2\text{Na}_2\text{Ir}_{0.5}\text{Os}_{0.5}\text{O}_4$ is much less compared to that of the undoped case, which can be very clearly seen from the DOS in Fig. 8(a). Therefore, in the case of $\text{Cs}_2\text{Na}_2\text{IrO}_4$, the SOC Hamiltonian couples the highest occupied and lowest unoccupied energy levels of two opposite spin channels, whereas for the Os-substituted compound, the SOC Hamiltonian couples the energy levels of the same spin channels. Thus the effect of the SOC interaction is very different at the Ir and Os sites. In the previous studies [49–51] the authors showed that the SOC matrix elements and the maximization of SOC eigenvalues are dependent on the electronic structure and the energy-level occupation. Also in the present cases, the changes of the easy axis before and after Os substitution are due to the fact that the SOC interactions are maximized differently due to the change in the electronic configurations.

VI. DISCUSSION AND CONCLUSION

We found that the discussed compound is very interesting and shows various unique magnetic properties which require further detailed experimental investigations. Since the iridates are not very responsive to neutron diffraction, which is the most obvious microscopic experimental tool to investigate such physics, muon spin resonance (μSR) measurement would turn out to be a more appropriate experimental tool to perform microscopic investigation of magnetism in the compound. As a guiding route to the experimentalists to understand the magnetism of this material microscopically, we provide the preliminary results of the spectroscopy measurement by calculating various probable muon active sites, using first-principles calculations. Muons are essentially active protons with a positive charge and interact with the system due to the presence of an intrinsic magnetic moment. Thus to mimic the presence of the μ^+ in the material, we added H atom sites in the structure and optimized the positions of H atoms, without any modifications at the other sites of the structure [52,53]. For the initial guess of the probable H site, we began by selecting symmetrically allowed positions near the anionic ligands. This was done keeping in mind that such positions experience maximum electronegativity. Figure 9(a) shows, post optimization eight possible μ^+ active sites, named $\mu^+(\text{I})$ to $\mu^+(\text{VIII})$. In Fig. 9(b) the distance between the μ^+ site with its nearest oxygen atom has been mentioned along with the relative energy per site. We found that the sites marked by II, III, and IV are energetically the most favorable positions to capture the μ^+ and act as the muon active sites. Although the other possible muon sites are energetically higher, the energy difference is very small—of the order of 0.5 eV.

In conclusion, our study focuses on a rare iridate, which is half-filled, and occurs in a square-planar environment with an intermediate spin state of $S = \frac{3}{2}$. We conducted detailed first-principles calculation studies of the electronic and magnetic properties of $\text{Cs}_2\text{Na}_2\text{IrO}_4$. From analyzing the phonon distortion modes, we provide a possible explanation of orthogonally

oriented IrO_4 square-planar geometry in the consecutive layers of the material, which is counterintuitive and also absent in its parent material Na_4IrO_4 . We found that in spite of the lack of structural connectivity via orthogonally oriented isolated IrO_4 moieties, a long-range canted AFM ground state is established due to weak spin-phonon coupling. The calculated mean-field magnetic transition temperature is very close to that of its parent counterpart. The most dominant exchange interactions are in the bc plane, between two perpendicularly oriented IrO_4 sites, suggesting the quasi-two-dimensional nature of magnetic interaction. We also found comparatively high MCA energy in this system, which can be further

enhanced by the 50% Os doping at the Ir sites. Further, we revealed that the origin of the large MCA is mostly electronic structure driven, which is additionally enhanced by the unique isolated square-planar geometry IrO_4 and can be understood as a second-order perturbative effect of SOC.

ACKNOWLEDGMENT

R.R. thanks IIT Goa for providing support from a research fellowship. S.K. acknowledges the Department of Science and Technology (DST), Government of India for providing INSPIRE research funding.

- [1] F. Bahrami, W. Lafargue-Dit-Hauret, O. I. Lebedev, R. Movshovich, H. Yang, D. Broido, X. Rocquefelte, and F. Tafti, Thermodynamic evidence of proximity to a Kitaev spin liquid in $\text{Ag}_3\text{LiIr}_2\text{O}_6$, *Phys. Rev. Lett.* **123**, 237203 (2019).
- [2] A. Chakraborty, V. Kumar, S. Bachhar, N. Büttgen, K. Yokoyama, P. K. Biswas, V. Siruguri, S. Pujari, I. Dasgupta, and A. V. Mahajan, Unusual spin dynamics in the low-temperature magnetically ordered state of $\text{Ag}_3\text{LiIr}_2\text{O}_6$, *Phys. Rev. B* **104**, 115106 (2021).
- [3] Z. Porter, P. M. Sarte, T. Petersen, M. H. Upton, L. Hozoi, and S. D. Wilson, Spin-orbit excitons and electronic configuration of the $5d^4$ insulator $\text{Sr}_3\text{Ir}_2\text{O}_7\text{F}_2$, *Phys. Rev. B* **106**, 115140 (2022).
- [4] A. B. Sushkov, J. B. Hofmann, G. S. Jenkins, J. Ishikawa, S. Nakatsuji, S. Das Sarma, and H. D. Drew, Optical evidence for a Weyl semimetal state in pyrochlore $\text{Eu}_2\text{Ir}_2\text{O}_7$, *Phys. Rev. B* **92**, 241108(R) (2015).
- [5] B. J. Kim, H. Jin, S. J. Moon, J. Y. Kim, B.-G. Park, C. S. Leem, J. Yu, T. W. Noh, C. Kim, S.-J. Oh, J.-H. Park, V. Durairaj, G. Cao, and E. Rotenberg, Novel $J_{\text{eff}} = 1/2$ Mott state induced by relativistic spin-orbit coupling in Sr_2IrO_4 , *Phys. Rev. Lett.* **101**, 076402 (2008).
- [6] E. Dagotto, Correlated electrons in high-temperature superconductors, *Rev. Mod. Phys.* **66**, 763 (1994).
- [7] V. V. Poltavets, K. A. Lokshin, S. Dikmen, M. Croft, T. Egami, and M. Greenblatt, $\text{La}_3\text{Ni}_2\text{IrO}_6$: A new double T' -type nickelate with infinite $\text{Ni}^{1+/2+}\text{O}_2$ layers, *J. Am. Chem. Soc.* **128**, 9050 (2006).
- [8] C. Tassel and H. Kageyama, Square planar coordinate iron oxides, *Chem. Soc. Rev.* **41**, 2025 (2012).
- [9] S. M. L. Teicher, L. K. Lamontagne, L. M. Schoop, and R. Seshadri, Fermi-level Dirac crossings in $4d$ and $5d$ cubic metal oxides: NaPd_3O_4 and NaPt_3O_4 , *Phys. Rev. B* **99**, 195148 (2019).
- [10] P. Kroeschell and R. Hoppe, Die koordinationszahl 4 bei Ir^{4+} : $\text{K}_4[\text{IrO}_4]$, *Naturwissenschaften* **72**, 442 (1985).
- [11] K. Mader and R. Hoppe, $\text{Cs}_4[\text{IrO}_4]$, ein neues iridat mit planarem anion $[\text{IrO}_4]^{4-}$, *Z. Anorg. Allg. Chem.* **614**, 30 (1992).
- [12] K. Mader and R. Hoppe, Zu Oxoiridaten mit quadratisch-planaren $[\text{IrO}_4]^{4-}$ -Gruppen: Na_4IrO_4 , eine MgO-Ersetzungsvariante mit geordneten Lücken im anionenteilgitter, *Z. Anorg. Allg. Chem.* **619**, 1647 (1993).
- [13] S. Kanungo, B. Yan, P. Merz, C. Felser, and M. Jansen, Na_4IrO_4 : Singular manifestation of square-planar coordination of a transition metal in d^5 configuration due to weak on-site Coulomb interaction, *Angew. Chem.* **127**, 5507 (2015).
- [14] X. Ming, C. Autieri, K. Yamauchi, and S. Picozzi, Role of square planar coordination in the magnetic properties of Na_4IrO_4 , *Phys. Rev. B* **96**, 205158 (2017).
- [15] D. Wang, F. Tang, Y. Du, and X. Wan, First-principles study of the giant magnetic anisotropy energy in bulk Na_4IrO_4 , *Phys. Rev. B* **96**, 205159 (2017).
- [16] K. Mader and R. Hoppe, Das erste caesium-haltige oxoiridat(IV): $\text{Cs}_2\text{Na}_2[\text{IrO}_4]$ mit quadratisch-planarer baugruppe $[\text{IrO}_4]^{4-}$, *J. Alloys Compd.* **183**, 198 (1992).
- [17] O. Muller and R. Roy, Synthesis and crystal chemistry of some new complex palladium oxides, *Adv. Chem.* **98**, 28 (1971).
- [18] S. Ichikawa and I. Terasaki, Metal-insulator transition in $\text{Ca}_{1-x}\text{Li}_x\text{Pd}_3\text{O}_4$, *Phys. Rev. B* **68**, 233101 (2003).
- [19] S. Obbade, N. Tancrét, F. Abraham, and E. Suard, Synthesis, electrical properties, and powder neutron crystal structure refinement of $\text{Pb}_{1-x}\text{Bi}_x\text{Pt}_2\text{O}_4$ compounds ($0 \leq x \leq 0.3$), *J. Solid State Chem.* **166**, 58 (2002).
- [20] K. B. Schwartz, C. T. Prewitt, R. D. Shannon, L. M. Corliss, J. M. Hastings, and B. L. Chamberland, Neutron powder diffraction study of two sodium platinum oxides: $\text{Na}_{1.0}\text{Pt}_3\text{O}_4$ and $\text{Na}_{0.73}\text{Pt}_3\text{O}_4$, *Acta Cryst.* **B 38**, 363 (1982).
- [21] J. P. Perdew, K. Burke, and M. Ernzerhof, Generalized gradient approximation made simple, *Phys. Rev. Lett.* **77**, 3865 (1996).
- [22] G. Kresse and J. Hafner, *Ab initio* molecular dynamics for liquid metals, *Phys. Rev. B* **47**, 558(R) (1993).
- [23] G. Kresse and J. Furthmüller, Efficient iterative schemes for *ab initio* total-energy calculations using a plane-wave basis set, *Phys. Rev. B* **54**, 11169 (1996).
- [24] V. I. Anisimov, I. V. Solovyev, M. A. Korotin, M. T. Czyzyk, and G. A. Sawatzky, Density-functional theory and NiO photoemission spectra, *Phys. Rev. B* **48**, 16929 (1993).
- [25] S. L. Dudarev, G. A. Botton, S. Y. Savrasov, C. J. Humphreys, and A. P. Sutton, Electron-energy-loss spectra and the structural stability of nickel oxide: An LSDA+U study, *Phys. Rev. B* **57**, 1505 (1998).
- [26] S. J. Moon, H. Jin, K. W. Kim, W. S. Choi, Y. S. Lee, J. Yu, G. Cao, A. Sumi, H. Funakubo, C. Bernhard, and T. W. Noh, Dimensionality-controlled insulator-metal transition and correlated metallic state in $5d$ transition metal oxides $\text{Sr}_{n+1}\text{Ir}_n\text{O}_{3n+1}$ ($n = 1, 2$, and ∞), *Phys. Rev. Lett.* **101**, 226402 (2008).

- [27] J. Sim, H. Yoon, S. H. Park, and M. J. Han, Calculating branching ratio and spin-orbit coupling from first principles: A formalism and its application to iridates, *Phys. Rev. B* **94**, 115149 (2016).
- [28] C. Martins, M. Aichhorn, L. Vaugier, and S. Biermann, Reduced effective spin-orbital degeneracy and spin-orbital ordering in paramagnetic transition-metal oxides: Sr_2IrO_4 versus Sr_2RhO_4 , *Phys. Rev. Lett.* **107**, 266404 (2011).
- [29] S. Bhowal, S. Baidya, I. Dasgupta, and T. Saha-Dasgupta, Breakdown of $J = 0$ nonmagnetic state in d^4 iridate double perovskites: A first-principles study, *Phys. Rev. B* **92**, 121113(R) (2015).
- [30] See Supplemental Material at <http://link.aps.org/supplemental/10.1103/PhysRevB.108.155110> for the variation of DOS, comparative energetics of different spin configurations, and magnetic exchange interactions with change in U_{eff} ; the evolution of MCA with scaling of the SOC strength; and phonon DOS by doping at the Ir site.
- [31] D. Hobbs, G. Kresse, and J. Hafner, Fully unconstrained noncollinear magnetism within the projector augmented-wave method, *Phys. Rev. B* **62**, 11556 (2000).
- [32] A. A. Mostofi, J. R. Yates, Y.-S. Lee, I. Souza, D. Vanderbilt, and N. Marzari, An updated version of wannier90: A tool for obtaining maximally-localised Wannier functions, *Comput. Phys. Commun.* **178**, 685 (2008).
- [33] A. Togo and I. Tanaka, First principles phonon calculations in materials science, *Scr. Mater.* **108**, 1 (2015).
- [34] Y. Tsujimoto, C. Tassel, N. Hayashi, T. Watanabe, H. Kageyama, K. Yoshimura, M. Takano, M. Ceretti, C. Ritter, and W. Paulus, Infinite-layer iron oxide with a square-planar coordination, *Nature (London)* **450**, 1062 (2007).
- [35] M. Rahman, Y.-Z. Nie, and G.-H. Guo, Electronic structures and magnetism of SrFeO_2 under pressure: A first-principles study, *Inorg. Chem.* **52**, 12529 (2013).
- [36] C. S. Hellberg, W. E. Pickett, L. L. Boyer, H. T. Stokes, and M. J. Mehl, Ab initio calculation of spin gap behavior in CaV_4O_9 , *J. Phys. Soc. Jpn.* **68**, 3489 (1999).
- [37] V. V. Mazurenko, F. Mila, and V. I. Anisimov, Electronic structure and exchange interactions of $\text{Na}_2\text{V}_3\text{O}_7$, *Phys. Rev. B* **73**, 014418 (2006).
- [38] H. J. Xiang, E. J. Kan, S. Wei, M. H. Whangbo, and X. G. Gong, Predicting the spin-lattice order of frustrated systems from first principles, *Phys. Rev. B* **84**, 224429 (2011).
- [39] S. Kanungo, B. Yan, M. Jansen, and C. Felser, *Ab initio* study of low-temperature magnetic properties of double perovskite $\text{Sr}_2\text{FeOsO}_6$, *Phys. Rev. B* **89**, 214414 (2014).
- [40] J. Sannigrahi, J. Sichelschmidt, B. Koo, A. Banerjee, S. Majumdar, and S. Kanungo, Microscopic investigation of low dimensional magnet $\text{Sc}_2\text{Cu}_2\text{O}_5$: Combined experimental and *ab initio* approach, *J. Phys.: Condens. Matter* **31**, 245802 (2019).
- [41] B. E. Prasad, S. Sadhukhan, T. C. Hansen, C. Felser, S. Kanungo, and M. Jansen, Synthesis, crystal and magnetic structure of the spin-chain compound Ag_2RuO_4 , *Phys. Rev. Mater.* **4**, 024418 (2020).
- [42] R. Roy and S. Kanungo, First principles investigation of spin-orbit coupling driven magnetism of the $3d-5d$ double-perovskite $(\text{Sr}/\text{Ca})_2\text{FeIrO}_6$, *Phys. Rev. B* **106**, 125113 (2022).
- [43] J. Samuel Smart, *Effective Field Theories of Magnetism* (W. B. Saunders Company, Philadelphia and London, 1966).
- [44] N. Marzari and D. Vanderbilt, Maximally localized generalized Wannier functions for composite energy bands, *Phys. Rev. B* **56**, 12847 (1997).
- [45] I. Souza, N. Marzari, and D. Vanderbilt, Maximally localized generalized Wannier functions for composite energy bands, *Phys. Rev. B* **65**, 035109 (2001).
- [46] M. A. Laguna-Marco, P. Kayser, J. A. Alonso, M. J. Martínez-Lope, M. van Veenendaal, Y. Choi, and D. Haskel, Electronic structure, local magnetism, and spin-orbit effects of Ir(IV)-, Ir(V)-, and Ir(VI)-based compounds, *Phys. Rev. B* **91**, 214433 (2015).
- [47] M. Jung, Y. Song, K. Lee, and W. E. Pickett, Structural and correlation effects in the itinerant insulating antiferromagnetic perovskite NaOsO_3 , *Phys. Rev. B* **87**, 115119 (2013).
- [48] S. Sarkar, S. Kanungo, and T. Saha-Dasgupta, *Ab initio* study of low-dimensional quantum spin systems $\text{Sr}_3\text{NiPtO}_6$, $\text{Sr}_3\text{CuPtO}_6$, and $\text{Sr}_3\text{NiIrO}_6$, *Phys. Rev. B* **82**, 235122 (2010).
- [49] H. Xiang, C. Lee, H. J. Koo, X. Gong, and M. H. Whangbo, Magnetic properties and energy-mapping analysis, *Dalton Trans.* **42**, 823 (2013).
- [50] D. Dai, H. Xiang, and M. H. Whangbo, Effects of spin-orbit coupling on magnetic properties of discrete and extended magnetic systems, *J. Comput. Chem.* **29**, 2187 (2008).
- [51] E. E. Gordon, H. Xiang, J. Köhler, and M. H. Whangbo, Spin orientations of the spin-half Ir^{4+} ions in $\text{Sr}_3\text{NiIrO}_6$, Sr_2IrO_4 , and Na_2IrO_3 : Density functional, perturbation theory, and Madelung potential analyses, *J. Chem. Phys.* **144**, 114706 (2016).
- [52] I. J. Onuorah, P. Bonfà, and R. D. Renzi, Muon contact hyperfine field in metals: A DFT calculation, *Phys. Rev. B* **97**, 174414 (2018).
- [53] K. J. A. Franke, B. M. Huddart, T. J. Hicken, F. Xiao, S. J. Blundell, F. L. Pratt, M. Crisanti, J. A. T. Barker, S. J. Clark, A. Štefančič, M. C. Hatnean, G. Balakrishnan, and T. Lancaster, Magnetic phases of skyrmion-hosting $\text{GaV}_4\text{S}_{8-y}\text{Se}_y$ ($y = 0, 2, 4, 8$) probed with muon spectroscopy, *Phys. Rev. B* **98**, 054428 (2018).